NANO LETTERS

pubs.acs.org/NanoLett
Letter

Near-Unity Absorption in Semiconductor Metasurfaces Using Kerker Interference

Sasan V. Grayli, Tarun Patel, Brad van Kasteren, Sathursan Kokilathasan, Burak Tekcan, Man Chun Alan Tam, William Fredrick Losin, Sarah Odinotski, Adam W. Tsen, Zbigniew R. Wasilewski, and Michael E. Reimer*

Cite This: *Nano Lett.* 2025, 25, 9362−9368

Read Online

ACCESS | Metrics & More | Article Recommendations | Supporting Information

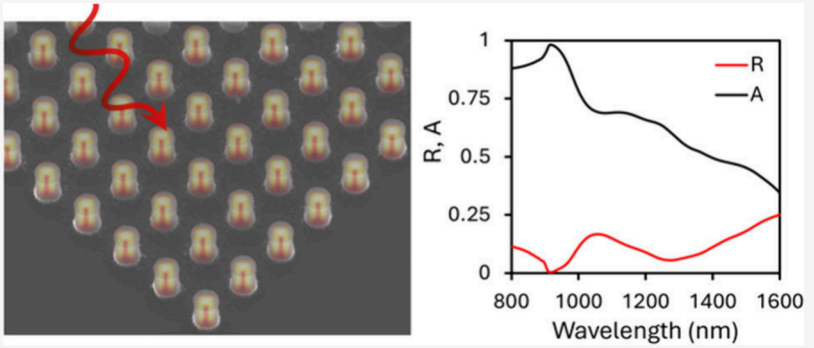

ABSTRACT: The ability to detect light with high efficiency is an important device metric for single-photon detectors and cameras, essential for applications ranging from quantum communication to biomedical imaging. However, these photodetectors have limited detection efficiency in the 850−1100 nm wavelength range, known as the 'valley of death'. Here, we demonstrate a near-perfect absorber in the 'valley of death' using a semiconductor metasurface with spectral and spatial selectivity on a high refractive index substrate. Our design leverages higher order optical modes of InGaAs resonators to generate Kerker interference at the target wavelength of 920 nm, which leads to a measured peak absorption efficiency of ∼94%. In addition, numerical calculations show that our design enables spatial control of the absorption profile within the resonators, which is promising for improving response time. Our approach offers tunability over a desired spectral range and paves the way for development of high-performance photodetectors.

KEYWORDS: *Kerker effect, metasurfaces, near-unity absorber, III−V semiconductors, multimode resonators, nanostructures*

Optical metasurfaces, comprising of dielectric and semiconductor resonators, have recently emerged to control the light-matter interaction in nanophotonic devices.[1−5] Controlling the magnetic and electric modes of guided light have created exciting opportunities for designing a new class of nanophotonic devices that can impact different areas of science and technologies ranging from biomedical imaging to quantum communication.[6−11] The remarkable functionality of all-dielectric metasurfaces in controlling the light-matter interaction at the nanoscale have led to the creation of flat optics, near-zero index waveguides and directional scatterers.[2−4,12] Enhanced absorption has been demonstrated with semiconductor metasurfaces,[8,13−21] which has improved the efficiency of solar cells[22] and photodetectors.[13,14,17] Meanwhile, a known shortcoming of current commercial semiconductor single-photon detectors and cameras is the detection efficiency in the wavelength band from 850 nm − 1100 nm, known as the 'valley of death', since this is where the detection efficiency of silicon (Si) and indium−gallium-arsenide (InGaAs)-based single-photon detectors and cameras have limited efficiency below 10%. This limited efficiency arises due to the need for fast response time in these photodetection and imaging applications, which necessitates a thin absorption layer. In Si, the absorption depth increases exponentially above 800 nm reducing absorption efficiency, while in III−V materials such as InGaAs the shorter wavelengths are absorbed close to the surface and the resulting charge carriers are not collected efficiently due to nonradiative recombination. This spectral region is of importance for cameras used in near-infrared imaging applications such as optical coherence tomography due to the necessary penetration depth of incident light in skin and fat tissues. Thus, there is an opportunity to

Received: March 19, 2025
Revised: May 9, 2025
Accepted: May 13, 2025
Published: June 2, 2025

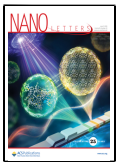

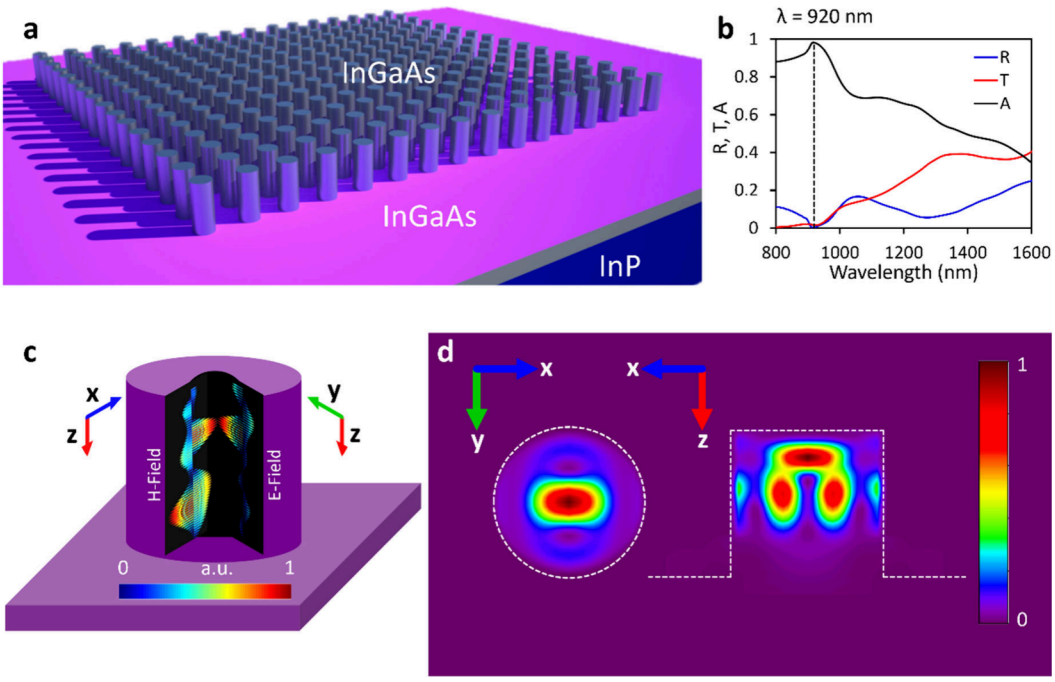

Figure 1. Near-unity absorption efficiency of a metasurface comprised of multimode InGaAs resonators on a high-index substrate. (a) 3D schematic view of multimode InGaAs resonators on a high-index InGaAs-InP substrate. (b) Calculated absorptance (A), reflectance (R) and transmittance (T) of the designed metasurface with 98% peak absorption efficiency at the target wavelength of λ = 920 nm. (c) Overlap of the magnetic (left) and electric (right) field within the multimode resonators. The electric and magnetic fields have been normalized and have been offset from the center for clarity. (d) Localized absorption profile in the $x-y$ plane (left) and $x-z$ plane (right) of the optimized multimode resonators (h = 960 nm, r = 230 nm and P = 900 nm) in a periodic lattice is shown for the target wavelength of 920 nm.

improve the device efficiency by incorporation of metasurface absorbers for next generation single-photon detectors and cameras.[23−27]

One of the most promising meta-optic approaches to realize a perfect absorber is by utilizing Huygens' metasurfaces that are constructed from semiconductor resonators.[2,3,8,13,19,28−31] Single disk-shaped resonators placed in a two-dimensional periodic array are among the most common geometrical designs that are used in semiconductor metasurface absorbers.[13,14,19] By controlling the diameter of the disk-shaped resonators, the first-order HE_{11} and EH_{11} hybrid modes can be spectrally overlapped.[13,14,19,32] This spectral overlap of the electric- and magnetic-dipoles in the semiconductor resonators leads to Kerker interference, in which backscattering is suppressed, and forward scattering is promoted.[33,34] Another approach to achieve Kerker interference is through the lattice resonances.[35,36] In these works, the magnetic (MLR) and electric (ELR) lattice resonant modes are tuned to spectrally overlap with the supported electric and magnetic dipoles of the resonators, respectively, to satisfy the Kerker condition.[19,35,36] Thus far, metasurface absorbers have been investigated through the design and fabrication of resonators embedded in low refractive index materials.[8,19] In this work, we demonstrate a near-unity metasurface absorber comprised of multimode InGaAs resonators fabricated on a high refractive index InGaAs-InP (indium-phosphide) substrate utilizing Kerker interference. We measure a peak absorption efficiency of 94% at the target design wavelength of 920 nm. Our simulations show that the Kerker interference in these multimode resonators leads to spatial localization of the absorption profile (~ 200 nm in diameter and ~ 300 nm along the height). Such localized absorption control can be leveraged to improve the timing resolution of single-photon detectors through minimizing spatial variation in the avalanche process of the photogenerated carriers.[17] Additionally, reduced volume of the absorption region can be utilized to minimize dark current.[37]

Up to now, narrowband semiconductor metasurfaces that demonstrated near-unity absorptance through Kerker interference were demonstrated in nanodisk resonators on a low refractive index substrate.[8,19,30] Supporting Information Notes 1 and 2 describe our analysis on such semiconductor metasurfaces. However, these narrowband metasurface absorbers cannot be easily incorporated in photodiode structures where the material layer stack requires high quality III−V semiconductors, commonly grown by molecular-beam epitaxy (MBE) and metal−organic chemical vapor deposition (MOCVD) (e.g., InGaAs). By placing these nanodisk resonators on a high refractive index substrate, the Kerker interference vanishes, leading to a loss of spectral selectivity and dramatic decline of the absorption efficiency. Our analysis on this effect of the nanodisk resonators on a high refractive index substrate is shown in Supporting Information Note 3. In these structures, the Kerker interference disappears since the fundamental modes (HE_{11} and EH_{11}) are no longer supported (see Supplementary Figure S2).

To restore Kerker interference in such resonators on a high-index substrate, larger multimode structures are required. Figure 1a depicts a 3D schematic view of our devices, which is an array of multimode InGaAs resonators on a high-index InGaAs-InP substrate. In Figure 1b, the calculated absorptance (A), reflectance (R) and transmittance (T) of our optimized multimode semiconductor metasurface is presented. The plot shows the suppression of backscattering (R < 0.3%) at the target wavelength of 920 nm, which is characteristic of Kerker interference. The transmittance has also been minimized

https://doi.org/10.1021/acs.nanolett.5c01777
Nano Lett. 2025, 25, 9362−9368

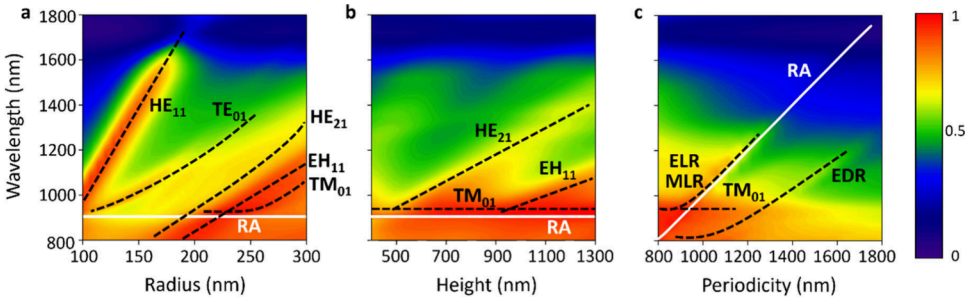

Figure 2. Kerker interference. (a)-(c) Illustrates the absorption contribution of optical modes (identified by dashed lines) in the multimode metasurface as a function of radius, height and periodicity, respectively. In (a), the presence of TE_{01} and TM_{01} modes are noticeable due to excitation by the electric and magnetic lattice resonances in the resonators with height of 960 nm and lattice periodicity of 900 nm. The overlap of TM_{01} with EH_{11} is noticeable for a radius of 230 nm, indicating maximum absorption resulting from Kerker interference. In (b), we observe that the increase in height of the resonator for a fixed radius of 230 nm and periodicity of 900 nm only shifts the HE_{21} and EH_{11} modes, while the TM_{01} remains constant. (c) Demonstrates the appearance of magnetic lattice resonance (MLR) and electric lattice resonance (ELR) for a metasurface comprised of resonators with height of 960 nm and radius of 230 nm. The color bar represents the normalized absorption efficiency. The Rayleigh anomaly (RA) is represented by the solid white line.

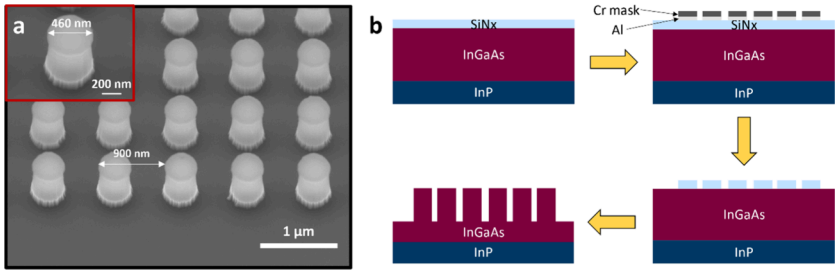

Figure 3. Fabrication of the InGaAs multimode Kerker metasurface absorber. (a) SEM image (tilt angle 30°) of the fabricated multimode resonators (h ≈ 960 nm) with 900 nm periodicity. The inset shows a single multimode resonator in which the diameter is measured to be 460 nm. (b) Fabrication process steps of the Kerker metasurface. The InGaAs film used to make the InGaAs resonators is 2000 nm thick.

indicating enhanced absorption. A peak absorptance of 98% is achieved at the target wavelength. Figure 1c illustrates the overlap of the electric and magnetic components of the excited modes in the resonator at 920 nm, which show that the electric and magnetic fields are in phase satisfying the conditions of Kerker interference. Moreover, this interference leads to the localization of the absorption profile as shown in Figure 1d. Here, the absorption profile shows that the maximum absorption occurs in a small region inside and on the axis of the resonators (<50 nm in diameter). We attribute this absorption characteristic of the resonator to the interference of the TM_{01} mode, excited by the magnetic lattice resonance, with the transverse electric component of the guided EH_{11} hybrid mode.

To identify the supported modes at 920 nm where near-unity absorption efficiency is achieved in Figure 1b, we perform eigenvalue modal analysis[38] of an infinitely long cylindrical resonator as a function of radius. See Supporting Information Note 4 for details of the modal analysis. Increasing the radius of the cylindrical resonator results in higher order modes to be supported, including transverse electric (TE) and magnetic (TM) modes.

To understand how Kerker interference is achieved in such multimode InGaAs resonators on a high-index substrate, we studied the effect of the resonator geometry (radius and height) and periodicity on the absorption efficiency using finite-difference time-domain (FDTD) numerical calculations (Figure 2). Details of the FDTD model and the effect of the optical modes on the absorptance of a single resonator are described in Supporting Information Note 5. To achieve modal overlap for Kerker interference we place the InGaAs resonators in a periodic array with a lattice constant (periodicity) of 900 nm for the optimized metasurface. The lattice constant of this metasurface was selected to be 900 nm to maintain the ratio of 0.51 between the resonator diameter (d) and the periodicity (P). We found that by adhering to this ratio, enhanced absorption in these InGaAs resonator metasurfaces can be achieved. Details of arriving to the d/P ratio of 0.51 to enhance absorption is described in Supporting Information Note 2. We also note that the initial estimate of the resonator diameter was obtained from the modal analysis (Figure S3a) where the cylinder diameter supports both the EH_{11} and TM_{01} modes with an effective refractive index >2.

Figure 2a and 2b illustrate the absorptance that arises from the coupling of light to different optical modes as the radius (Figure 2a) and height (Figure 2b) of the resonators are varied. The two transverse modes, TE_{01} and TM_{01}, appear as a consequence of being excited by the lattice resonance modes (ELR and MLR). Among the two transverse modes, TM_{01} is of particular importance since it overlaps with the EH_{11} mode at a radius of 230 nm and height of 960 nm leading to the highest absorption efficiency of 98% at $\lambda \approx 920$ nm. At this intersection of the TM_{01} and EH_{11} modes, it is the transverse component of the electric field in the EH_{11} mode that overlaps with the TM_{01} mode for Kerker interference. We find that changing the height only impacts the HE_{21} and EH_{11} modes, while the TM_{01} mode remains constant. In contrast, changing the radius can tune both hybrid and transverse modes.

To better understand how the periodicity impacts the lattice resonant modes, we studied the absorptance as a function of

https://doi.org/10.1021/acs.nanolett.5c01777
Nano Lett. 2025, 25, 9362−9368

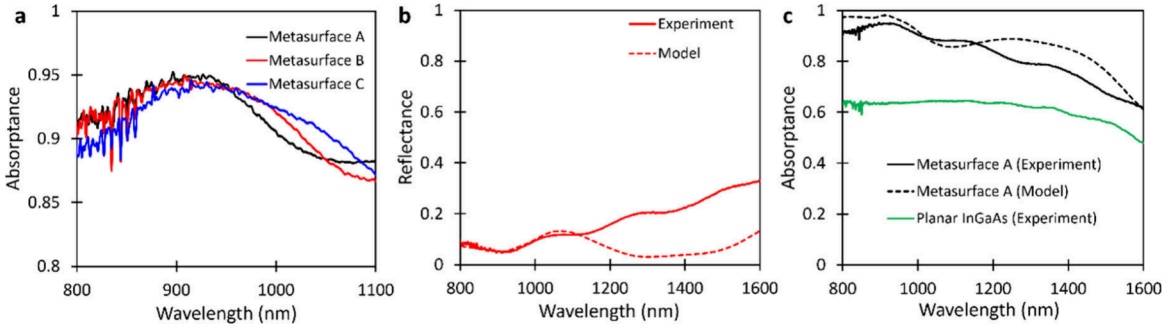

Figure 4. Experimental results of perfect metasurface absorber. (a) Measured absorptance of the three fabricated metasurfaces with different periodicities and resonator diameters. Metasurface A: P = 900 nm $d_{top} \approx$ 420 nm and $d_{bottom} \approx$ 450 nm; Metasurface B: P = 960 nm and $d_{top} \approx$ 425 nm and $d_{bottom} \approx$ 470 nm; Metasurface C: P = 1030 nm and $d_{top} \approx$ 475 nm and $d_{bottom} \approx$ 525 nm. (b) Measured (solid red line) and modeled (dashed red line) reflectance of Metasurface A. (c) Experimental (solid black line) and numerically calculated (dashed black line) absorptance of Metasurface A is compared with the measured absorptance of the planar InGaAs with no metasurface (solid green line).

the resonators' separation for a fixed height of 960 nm and radius of 230 nm. The results of our numerical calculations are plotted in Figure 2c. In this case, the increase in periodicity leads to shifting both the MLR and ELR to longer wavelengths simultaneously. As the periodicity becomes larger, the absorption efficiency gradually drops as the MLR is no longer effectively exciting the TM_{01} mode. In Supplementary Figure S4 we show how the changes of the resonator's radius, height and periodicity, impacts the reflectance of the metasurface absorber.

Using the optimized resonator dimensions from the previous section, we fabricated the metasurface absorber in a 2000 nm InGaAs film that was grown on an InP wafer using MBE. The fabricated metasurface absorber is depicted in the scanning electron microscope (SEM) image of Figure 3a, consisting of a 100 μm × 100 μm array of InGaAs resonators with a measured height of 960 nm, periodicity of 900 nm and diameter of 460 nm.

Figure 3b depicts the fabrication steps for realizing the InGaAs metasurface absorber. In our process, we first deposit a 500 nm thick silicon nitride (SiN_x) film to be used as the hard mask. To make resonators with smooth sidewalls, we use e-beam lithography and a lift-off process to make an Al/Cr mask that transfers the desired pattern onto the SiN_x hard mask. An Oxford inductive coupled plasma-reactive ion etching (ICP-RIE) tool is then used to fabricate the InGaAs resonators using the SiN_x hard mask (see Supporting Information Note 7 for further details). The smooth sidewalls achieved during our fabrication process for the InGaAs resonators is evident in the SEM image of Figure 3a. We concluded the fabrication process by removing the remaining SiN_x mask through a buffered oxide etch.

To assess the absorption efficiency of the fabricated metasurface absorber, we performed Fourier Transform Infrared (FTIR) spectroscopy to measure the reflectance (R) and transmittance (T) in the wavelength range from 800 to 1600 nm. Details of the FTIR measurements can be found in Supporting Information Note 8. We then calculated the absorptance (A) from the relation, A = 1 − R − T. Figure 4a shows the measured absorptance of three fabricated metasurface absorbers with increasing diameter and periodicity for a designed peak absorptance at 920 nm (metasurface A), 980 nm (metasurface B) and 1060 nm (metasurface C). The fabricated nanostructure dimensions for these target wavelengths are given in the figure caption. We focus our attention on metasurface A as the resonators have minimal tapering and closely resemble our target design dimensions from Figure 1.

The observed peaks are broader than expected (see Figure 1b for expected metasurface A absorptance spectrum for light at normal incidence). To account for the broader measured absorptance peak around 920 nm for metasurface A, we included the effect of the objective used in the measurements, which has a numerical aperture (NA) of 0.5. This NA focuses light with an incident angle ranging from −30° to +30° on the resonators. We thus calculated the average reflectance (absorptance) in the simulations by varying the incident angle from −30° to +30°. The calculated average reflectance and absorptance spectra using this updated model are shown in Figure 4b and Figure 4c, respectively. The observed broadening in the reflectance and absorptance spectrum is due to excitation of higher order azimuthal modes in the cylindrical resonators. The simulations now show better quantitative agreement with the measurements at the target wavelength of 920 nm. The details of these simulations are included in Supplementary Note 9. Nonetheless, the observed absorptance for all three metasurfaces in Figure 4a are >90% from 800 to 1000 nm, with peak absorptance of ∼95%. This peak absorptance is also evident in the reflectance minima of 5% for metasurface A as shown in Figure 4b. For comparison, we also measured the absorptance of an unpatterned InGaAs film with comparable thickness (2000 nm) to the resonators. The measurement is plotted in Figure 4c, demonstrating an average absorptance of 62% from 800 to 1600 nm, which is significantly less than the fabricated metasurface absorbers at 920 nm.

For metasurface B and C, the peak of maximum absorptance is further broadened as compared to metasurface A, likely due to excessive tapering of the larger diameter resonators (see Supplementary Note 10 for SEM images and additional details). Regardless, compared to metasurface A we observe additional absorptance around 960 and 1030 nm indicating the redshift of the Kerker interference as expected. We also note that the deviation of the model from experiment at longer wavelengths beyond 1100 nm (Figure 4b and Figure 4C) could be due to the fabrication imperfections such as surface roughness of the substrate and the resonators, and unwanted tapering that was introduced during the RIE process (see Supplementary Figure S8). The effects of surface roughness and unwanted tapering can be mitigated in future devices by

https://doi.org/10.1021/acs.nanolett.5c01777
Nano Lett. 2025, 25, 9362−9368

additional fabrication steps such as digital cycle etching and optimized RIE recipes.

We designed a perfect semiconductor metasurface absorber on a high-index substrate and experimentally demonstrated near-unity absorption efficiency on devices with varying diameter and periodicity. The fabricated metasurface that closely matched our target dimensions showed spectral selectivity at 920 nm with a peak absorption efficiency of 94%. This was achieved through Kerker interference by overlapping of the EH_{11} and TM_{01} higher order optical modes. Previous work with resonators on a low-index substrate achieved the Kerker condition with an impressive peak absorptance of 60% at 1550 nm[19] and >90% peak absorptance in the near-infrared around 800 nm.[8] Our work realizes Kerker interference in a high-index metasurface for the first time, compatible for developing high-performance photodetectors.

The presented metasurface absorber with near-unity efficiency is a promising platform to be used as the active region of a photodetector based on III−V semiconductors. Enhancing photodetector performance through near-unity absorption in the valley of death region can aid in biomedical imaging. In addition, we showed that devices can be tailored to control the spatial location of absorption in the metasurface absorber. One main advantage that arises from localized absorption is that the thickness of the absorption region in avalanche photodiodes, typically made out of small bandgap semiconductors, such as InGaAs, can be reduced without sacrificing the absorption efficiency.[37] The reduced device thickness will aid in faster response time in single-photon detectors, while the in-plane localization can help in improving the timing resolution of single-photon detectors.[17] Importantly, this improved timing resolution will be achieved simultaneously with increased absorption efficiency compared to planar single-photon detectors. Such enhanced single-photon detector performance is essential for photonic quantum computing, communication, sensing, and imaging.

■ ASSOCIATED CONTENT

Data Availability Statement

The data that support the plots within this paper and other findings of this study are available from the corresponding author upon reasonable request.

Supporting Information

The Supporting Information is available free of charge at https://pubs.acs.org/doi/10.1021/acs.nanolett.5c01777.

Additional information on the simulations for Kerker metasurfaces, effect of high-index substrate on nanodisks, details of modal analysis, the method of designing multimode resonators, details of numerical calculations for reflectance, fabrication details, optical measurement details, effect of incident angle on the absorptance, effect of tapering on spectral broadening around the Kerker resonance and measured complex refractive index of InGaAs used in the simulations (PDF)

■ AUTHOR INFORMATION

Corresponding Author

Michael E. Reimer − *Institute for Quantum Computing, University of Waterloo, Waterloo, ON N2L 3G1, Canada; Department of Electrical and Computer Engineering, University of Waterloo, Waterloo, ON N2L 3G1, Canada;* Email: mreimer@uwaterloo.ca

Authors

Sasan V. Grayli − *Institute for Quantum Computing, University of Waterloo, Waterloo, ON N2L 3G1, Canada; Department of Electrical and Computer Engineering, University of Waterloo, Waterloo, ON N2L 3G1, Canada;* orcid.org/0000-0001-9149-8294

Tarun Patel − *Institute for Quantum Computing, University of Waterloo, Waterloo, ON N2L 3G1, Canada; Department of Electrical and Computer Engineering, University of Waterloo, Waterloo, ON N2L 3G1, Canada*

Brad van Kasteren − *Institute for Quantum Computing, University of Waterloo, Waterloo, ON N2L 3G1, Canada; Department of Electrical and Computer Engineering, University of Waterloo, Waterloo, ON N2L 3G1, Canada*

Sathursan Kokilathasan − *Institute for Quantum Computing, University of Waterloo, Waterloo, ON N2L 3G1, Canada; Department of Electrical and Computer Engineering, University of Waterloo, Waterloo, ON N2L 3G1, Canada;* orcid.org/0000-0002-1572-8702

Burak Tekcan − *Institute for Quantum Computing, University of Waterloo, Waterloo, ON N2L 3G1, Canada; Department of Electrical and Computer Engineering, University of Waterloo, Waterloo, ON N2L 3G1, Canada*

Man Chun Alan Tam − *Institute for Quantum Computing, University of Waterloo, Waterloo, ON N2L 3G1, Canada; Department of Electrical and Computer Engineering, University of Waterloo, Waterloo, ON N2L 3G1, Canada; Waterloo Institute for Nanotechnology, University of Waterloo, Waterloo, ON N2L 3G1, Canada;* orcid.org/0000-0002-6749-9606

William Fredrick Losin − *Institute for Quantum Computing, University of Waterloo, Waterloo, ON N2L 3G1, Canada; Department of Electrical and Computer Engineering, University of Waterloo, Waterloo, ON N2L 3G1, Canada*

Sarah Odinotski − *Institute for Quantum Computing, University of Waterloo, Waterloo, ON N2L 3G1, Canada; Department of Electrical and Computer Engineering, University of Waterloo, Waterloo, ON N2L 3G1, Canada*

Adam W. Tsen − *Institute for Quantum Computing, University of Waterloo, Waterloo, ON N2L 3G1, Canada; Department of Chemistry, University of Waterloo, Waterloo, ON N2L 3G1, Canada*

Zbigniew R. Wasilewski − *Department of Electrical and Computer Engineering, University of Waterloo, Waterloo, ON N2L 3G1, Canada; Waterloo Institute for Nanotechnology, University of Waterloo, Waterloo, ON N2L 3G1, Canada;* orcid.org/0000-0001-7116-5863

Complete contact information is available at: https://pubs.acs.org/10.1021/acs.nanolett.5c01777

Author Contributions

S.V.G. and M.E.R. wrote the manuscript with input from T.P. S.V.G. designed, simulated and fabricated the nanostructures. A.W.T. supplied the FTIR spectrometer for absorption measurements, carried out by T.P. S.K. did the modal analysis. S.V.G. fabricated the samples with help of S.O. and B.T. The InGaAs film on an InP wafer was supplied by Z.W., grown by M.C.T. B.K. and W.L. aided in the simulations.

Notes

The authors declare no competing financial interest.

https://doi.org/10.1021/acs.nanolett.5c01777
Nano Lett. 2025, 25, 9362−9368

■ ACKNOWLEDGMENTS

This research was undertaken thanks in part to funding from the Canada First Research Excellence Fund. This work was also supported by the Natural Sciences and Engineering Research Council of Canada (NSERC) Quantum Alliance, Ontario Research Fund: Research Excellence (ORF-RE) and Mitacs. Moreover, the University of Waterloo's QNFCF facility was used for this work. This infrastructure would not be possible without the significant contributions of CFREF-TQT, CFI, ISED, the Ontario Ministry of Research & Innovation and Mike & Ophelia Lazaridis. Their support is gratefully acknowledged.

■ REFERENCES

(1) Schuller, J. A.; Zia, R.; Taubner, T.; Brongersma, M. L. Dielectric Metamaterials Based on Electric and Magnetic Resonances of Silicon Carbide Particles. *Phys. Rev. Lett.* **2007**, *99* (10), 107401.
(2) Staude, I.; Miroshnichenko, A. E.; Decker, M.; Fofang, N. T.; Liu, S.; Gonzales, E.; Dominguez, J.; Luk, T. S.; Neshev, D. N.; Brener, I.; Kivshar, Y. Tailoring Directional Scattering through Magnetic and Electric Resonances in Subwavelength Silicon Nanodisks. *ACS Nano* **2013**, *7* (9), 7824−7832.
(3) Pfeiffer, C.; Grbic, A. Metamaterial Huygens' Surfaces: Tailoring Wave Fronts with Reflectionless Sheets. *Phys. Rev. Lett.* **2013**, *110* (19), 197401.
(4) Kamali, S. M.; Arbabi, E.; Arbabi, A.; Faraon, A. A Review of Dielectric Optical Metasurfaces for Wavefront Control. *Nanophotonics* **2018**, *7* (6), 1041−1068.
(5) Jahani, S.; Jacob, Z. All-Dielectric Metamaterials. *Nat. Nanotechnol.* **2016**, *11* (1), 23−36.
(6) Zhang, S.; Wong, C. L.; Zeng, S.; Bi, R.; Tai, K.; Dholakia, K.; Olivo, M. Metasurfaces for Biomedical Applications: Imaging and Sensing from a Nanophotonics Perspective. *Nanophotonics* **2020**, *10* (1), 259−293.
(7) Zheng, C.; Wang, G.; Li, J.; Li, J.; Wang, S.; Zhao, H.; Li, M.; Yue, Z.; Zhang, Y.; Zhang, Y.; Yao, J. All-Dielectric Metasurface for Manipulating the Superpositions of Orbital Angular Momentum via Spin-Decoupling. *Advanced Optical Materials* **2021**, *9* (10), 2002007.
(8) Mitrofanov, O.; Hale, L. L.; Vabishchevich, P. P.; Luk, T. S.; Addamane, S. J.; Reno, J. L.; Brener, I. Perfectly Absorbing Dielectric Metasurfaces for Photodetection. *APL Photonics* **2020**, *5* (10), 101304.
(9) Bao, Y.; Lin, Q.; Su, R.; Zhou, Z.-K.; Song, J.; Li, J.; Wang, X.-H. On-Demand Spin-State Manipulation of Single-Photon Emission from Quantum Dot Integrated with Metasurface. *Science Advances* **2020**, *6* (31), No. eaba8761.
(10) Georgi, P.; Massaro, M.; Luo, K.-H.; Sain, B.; Montaut, N.; Herrmann, H.; Weiss, T.; Li, G.; Silberhorn, C.; Zentgraf, T. Metasurface Interferometry toward Quantum Sensors. *Light Sci. Appl.* **2019**, *8* (1), 70.
(11) Yavas, O.; Svedendahl, M.; Quidant, R. Unravelling the Role of Electric and Magnetic Dipoles in Biosensing with Si Nanoresonators. *ACS Nano* **2019**, *13* (4), 4582−4588.
(12) Dong, T.; Liang, J.; Camayd-Muñoz, S.; Liu, Y.; Tang, H.; Kita, S.; Chen, P.; Wu, X.; Chu, W.; Mazur, E.; Li, Y. Ultra-Low-Loss on-Chip Zero-Index Materials. *Light Sci. Appl.* **2021**, *10* (1), 10.
(13) Fan, K.; Suen, J. Y.; Liu, X.; Padilla, W. J. All-Dielectric Metasurface Absorbers for Uncooled Terahertz Imaging. *Optica, OPTICA* **2017**, *4* (6), 601−604.
(14) Liu, X.; Fan, K.; Shadrivov, I. V.; Padilla, W. J. Experimental Realization of a Terahertz All-Dielectric Metasurface Absorber. *Opt. Express, OE* **2017**, *25* (1), 191−201.
(15) Ming, X.; Liu, X.; Sun, L.; Padilla, W. J. Degenerate Critical Coupling in All-Dielectric Metasurface Absorbers. *Opt. Express, OE* **2017**, *25* (20), 24658−24669.
(16) Liao, Y.-L.; Zhao, Y. Ultra-Narrowband Dielectric Metamaterial Absorber with Ultra-Sparse Nanowire Grids for Sensing Applications. *Sci. Rep* **2020**, *10* (1), 1480.
(17) Gibson, S. J.; van Kasteren, B.; Tekcan, B.; Cui, Y.; van Dam, D.; Haverkort, J. E. M.; Bakkers, E. P. A. M.; Reimer, M. E. Tapered InP Nanowire Arrays for Efficient Broadband High-Speed Single-Photon Detection. *Nat. Nanotechnol.* **2019**, *14* (5), 473−479.
(18) Wang, B.; Leu, P. W. Enhanced Absorption in Silicon Nanocone Arrays for Photovoltaics. *Nanotechnology* **2012**, *23* (19), 194003.
(19) Zhou, Z.-X.; Ye, M.-J.; Yu, M.-W.; Yang, J.-H.; Su, K.-L.; Yang, C.-C.; Lin, C.-Y.; Babicheva, V. E.; Timofeev, I. V.; Chen, K.-P. Germanium Metasurfaces with Lattice Kerker Effect in Near-Infrared Photodetectors. *ACS Nano* **2022**, *16* (4), 5994−6001.
(20) Huang, Z.; Wang, J.; Jia, W.; Zhang, S.; Zhou, C. All-Dielectric Metasurfaces Enabled by Quasi-BIC for High-Q near-Perfect Light Absorption. *Opt. Lett., OL* **2025**, *50* (1), 105−108.
(21) Fan, K.; Shadrivov, I. V.; Miroshnichenko, A. E.; Padilla, W. J. Infrared All-Dielectric Kerker Metasurfaces. *Opt. Express, OE* **2021**, *29* (7), 10518−10526.
(22) van Dam, D.; van Hoof, N. J. J.; Cui, Y.; van Veldhoven, P. J.; Bakkers, E. P. A. M.; Gómez Rivas, J.; Haverkort, J. E. M. High-Efficiency Nanowire Solar Cells with Omnidirectionally Enhanced Absorption Due to Self-Aligned Indium-Tin-Oxide Mie Scatterers. *ACS Nano* **2016**, *10* (12), 11414−11419.
(23) Smith, A. M.; Mancini, M. C.; Nie, S. Second Window for in Vivo Imaging. *Nat. Nanotechnol.* **2009**, *4* (11), 710−711.
(24) Weissleder, R. A Clearer Vision for in Vivo Imaging. *Nat. Biotechnol.* **2001**, *19* (4), 316−317.
(25) Owens, E. A.; Lee, S.; Choi, J.; Henary, M.; Choi, H. S. NIR Fluorescent Small Molecules for Intraoperative Imaging. *WIREs Nanomedicine and Nanobiotechnology* **2015**, *7* (6), 828−838.
(26) Sajedi, S.; Sabet, H.; Choi, H. S. Intraoperative Biophotonic Imaging Systems for Image-Guided Interventions. *Nanophotonics* **2018**, *8* (1), 99−116.
(27) Hong, G.; Antaris, A. L.; Dai, H. Near-Infrared Fluorophores for Biomedical Imaging. *Nat. Biomed Eng.* **2017**, *1* (1), 1−22.
(28) Decker, M.; Staude, I.; Falkner, M.; Dominguez, J.; Neshev, D. N.; Brener, I.; Pertsch, T.; Kivshar, Y. S. High-Efficiency Dielectric Huygens' Surfaces. *Advanced Optical Materials* **2015**, *3* (6), 813−820.
(29) He, Y.; Deng, H.; Jiao, X.; He, S.; Gao, J.; Yang, X. Infrared Perfect Absorber Based on Nanowire Metamaterial Cavities. *Opt. Lett., OL* **2013**, *38* (7), 1179−1181.
(30) Hale, L. L.; Vabishchevich, P. P.; Vabishchevich, P. P.; Vabishchevich, P. P.; Siday, T.; Siday, T.; Harris, C. T.; Harris, C. T.; Luk, T. S.; Luk, T. S.; Addamane, S. J.; Addamane, S. J.; Reno, J. L.; Reno, J. L.; Brener, I.; Brener, I.; Mitrofanov, O.; Mitrofanov, O. Perfect Absorption in GaAs Metasurfaces near the Bandgap Edge. *Opt. Express, OE* **2020**, *28* (23), 35284−35296.
(31) Zhang, X.; Li, J.; Donegan, J. F.; Bradley, A. L. Constructive and Destructive Interference of Kerker-Type Scattering in an Ultrathin Silicon Huygens Metasurface. *Phys. Rev. Mater.* **2020**, *4* (12), 125202.
(32) van de Groep, J.; Polman, A. Designing Dielectric Resonators on Substrates: Combining Magnetic and Electric Resonances. *Opt. Express, OE* **2013**, *21* (22), 26285−26302.
(33) Kerker, M.; Wang, D.-S.; Giles, C. L. Electromagnetic Scattering by Magnetic Spheres. *J. Opt. Soc. Am., JOSA* **1983**, *73* (6), 765−767.
(34) Liu, W.; Kivshar, Y. S. Generalized Kerker Effects in Nanophotonics and Meta-Optics; *Opt. Express, OE* **2018**, *26* (10), 13085−13105.
(35) Babicheva, V. E.; Evlyukhin, A. B. Resonant Lattice Kerker Effect in Metasurfaces with Electric and Magnetic Optical Responses. *Laser & Photonics Reviews* **2017**, *11* (6), 1700132.
(36) Babicheva, V. E.; Moloney, J. V. Lattice Effect Influence on the Electric and Magnetic Dipole Resonance Overlap in a Disk Array. *Nanophotonics* **2018**, *7* (10), 1663−1668.
(37) Chen, D.; March, S. D.; Jones, A. H.; Shen, Y.; Dadey, A. A.; Sun, K.; McArthur, J. A.; Skipper, A. M.; Xue, X.; Guo, B.; Bai, J.;

https://doi.org/10.1021/acs.nanolett.5c01777
Nano Lett. 2025, 25, 9362−9368

Bank, S. R.; Campbell, J. C. Photon-Trapping-Enhanced Avalanche Photodiodes for Mid-Infrared Applications. *Nat. Photonics* **2023**, *17* (7), 594−600.

(38) Snyder, A. W. *Optical Waveguide Theory*, 1st ed. 1983.; Science paperbacks; Springer US: New York, NY, 1983. DOI: 10.1007/978-1-4613-2813-1.

https://doi.org/10.1021/acs.nanolett.5c01777
Nano Lett. 2025, 25, 9362−9368